An interval of high salinity in ancient Gale crater lake on Mars

W. Rapin, B. Ehlmann, G. Dromart, J. Schieber, N. Thomas, W. W Fischer, V. Fox, N. Stein, M. Nachon, B. C Clark, et al.

Title: An interval of high salinity in ancient Gale crater lake, Mars

Authors: W. Rapin[1], B. L. Ehlmann[1,2], G. Dromart[3], J. Schieber[4], N. H. Thomas[1], W. W. Fischer[1], V. K. Fox[1], N. T. Stein[1], M. Nachon[5], B. C. Clark[6], L. C. Kah[7], L. Thompson[8], H. A. Meyer[1], T. S. J. Gabriel[9], C. Hardgrove[9], N. Mangold[10], F. Rivera Hernandez[11], R. C. Wiens[12], A. R. Vasavada[2]

[1]California Institute of Technology, Pasadena, CA; [2]Jet Propulsion Laboratory, California Institute of Technology, Pasadena, CA; [3]Laboratoire de Géologie de Lyon, Université de Lyon, France; [4]Indiana University, Bloomington, IN; [5]Texas A&M University, College Station, TX; [6]Space Science Institute, Boulder, CO; [7]University of Tennessee, Knoxville, TN; [8]University of New Brunswick, Canada; [9]School of Earth and Space Exploration, Arizona State University, Tempe, AZ; [10]Laboratoire de Planétologie et Géodynamique, UMR6112, CNRS, Université Nantes, Université Angers, France; [11]Dartmouth College, Hanover, NH; [12]Los Alamos National Laboratory, Los Alamos, NM.

Abstract/First Parag.

Precipitated minerals, including salts, are primary tracers of atmospheric conditions and water chemistry in lake basins. Ongoing *in situ* exploration by the Curiosity rover of a thick section of Hesperian (~3.3-3.7 Ga) sedimentary rocks within Gale crater has revealed clay-bearing fluvio-lacustrine deposits with sporadic sulfate occurrences primarily as late-stage diagenetic veins and concretions. Here, we report the discovery of bulk enrichments, disseminated in the bedrock, of Ca-sulfate (30-50 wt%) that occur intermittently over ~150 m of stratigraphy and hydrated Mg-sulfate (26-36 wt%) within a thinner section of strata. We use geochemical analysis, primarily from the ChemCam laser-induced breakdown spectrometer (LIBS) and combined with results from other rover instruments, to characterize the enrichments and their lithology. The deposits are consistent with early diagenetic, pre-compaction, salt

precipitation from brines concentrated by evaporation, including Mg-sulfate rich brines indicating extreme evaporative concentration. This saline interval represents a significant hydrologic perturbation affecting the lake basin, and possibly reflecting variations in obliquity and orbital parameters of the planet. Our findings support a stepwise change in Mars' Hesperian climate towards more arid and sulfate-dominated environments inferred from orbital observations.

Carbonate, chloride, and sulfate salts provide geochemical fingerprints of the past chemistry of terrestrial lake basins. On Mars, such chemical sediments reflect systematic differences in dissolved ions that lead to distinctive chemical divides and mineral assemblages[1]. For example, *in situ*, widespread Mg/Ca/Fe-sulfate enrichments within aeolian and interdune playa sediments at Meridiani Planum have been interpreted to have formed from acidic and saline early diagenetic brines[2]. Low CO_3^{2-}, high SO_4^{2-}, and low pH waters enriched in Fe(II) formed a unique assemblage of hydrated sulfate minerals, jarosite, silica, and chloride minerals[3]. Under less acidic conditions, iron is relatively immobile, Ca/Mg-sulfate and chloride assemblages are favored, and carbonate minerals can form under sufficiently elevated CO_3^{2-} concentrations[1].

From orbit, a diversity of sulfate, carbonate, and chloride salts is observed on Mars, reflecting fluid chemistries that varied both spatially and temporally[4]. Thick layered sulfate deposits are observed at a number of late Noachian to late Hesperian locations (~3.5 Ga). Their apparent absence in the older stratigraphic record is hypothesized to reflect the diminishing availability of liquid water on Mars[5]. Gale crater provides an exemplary sedimentary succession dated to the Hesperian[6] that contains clay minerals transitioning to sulfate minerals over ~300 m of stratigraphy[7,8]. Understanding the reason for this transition is one of the primary objectives of the MSL/Curiosity rover investigation. So far, the rover has explored clay-bearing fluvio-lacustrine sedimentary record in the lowermost stratigraphy which is dominated by

the formation of mineral assemblages that include authigenic or detrital clay minerals and iron oxides[9–12], with a potentially punctuated transition in redox state[10]. Sulfates have been observed mostly as abundant late diagenetic Ca-sulfate fracture-fills[13,14], and inferred from crystal pseudomorphs after gypsum that occur locally in the lowermost Murray formation[15]. Mg-sulfate were also observed, but primarily associated with sparse diagenetic features, such as concretions and dendrites[10,16,17].

Here we detail the chemistry of lacustrine deposits from the upper Murray formation heterolithic facies which consists of interbedded sandstone and mudstone with exposures dominated by broken, tilted blocks with diverse resistance to erosion. This change in sedimentary facies in the Murray formation correlates with a gradual transition in the bedrock alteration index defined by major element compositions[18]. It also coincides with an increase in the prevalence of S, Cl and associated salts which suggest the presence of distinctively saline waters.

Ca-sulfate bedrock enrichment

Starting at the base of the Sutton Island member (Figure 1-a), enrichment of Ca-sulfate is observed within the bulk sedimentary bedrock, distinct from prior occurrences in fracture fills and merely sporadic detections (targets with <50% of points enriched). Bulk enrichments are characterized by ChemCam analyses of bedrock, where the majority of sampled points exhibit compositions that correspond to binary mixtures of typical Murray bedrock (i.e. average sulfate-free bedrock dominated by silicate minerals, with an average CaO content ~1.6 wt%) with 30 to 50 wt% of a Ca-sulfate end-member (Figure 2-a; see also Figure S1 and Table S1). For such concentrations, the S signal is clearly expressed in emission spectra by 3 peaks at 543 nm, 545 nm, and 564 nm, leading to a ~0.2 nm shift in the location of peak centroids at 543 nm and 545 nm, combined with an increase in the magnitude of the 564-nm peak emission (Figure S2), as is observed in laboratory experiments[19]. Independent measurement by the Alpha Particle X-ray

Spectrometer (APXS) at the centimeter-scale also record bulk CaO enrichments of the Murray bedrock that are correlated with SO_3 content, toward the $CaSO_4$ end-member (Figure S3).

Ca-sulfate corresponding to bedrock enrichment excludes contribution from mineralized veins identified from images taken at <0.5mm/pixel using the ChemCam Remote Micro Imager (RMI). In the absence of vein contribution, the repeated enrichment in the majority of observation points within both sandstone and mudstone targets indicates that the enrichment is disseminated within the bulk rock (Table S1; Figure 3). In general, the mudstone is laminated[20]; however, intervals with Ca-sulfate enrichment are commonly more resistant to erosion and display nodular or massive textures (Figure 3, S4 and S5). Where close-up images (< 100 µm/pixel) are available, these intervals do not show veins (Figure 3-e), although in some cases, submillimeter white grains (Figure 3-f) or elongate euhedral crystals associated with crystal molds (Figure 3-g) were observed. Bulk enrichment occurs at several discrete elevations between -4370 m and -4200 m in the stratigraphy of the upper Murray formation, contrasting with only sporadic enrichment detected elsewhere in the formation (Figure 1-b).

The association of calcium with carbonate, which neither ChemCam or APXS can directly detect, cannot be entirely ruled out (Figure 2-a shows that bedrock CaO content increases up to ~8 wt% while sulfur remains below detection limit which could allow for up to ~12 wt% calcite). Yet X-ray diffraction analyses on Murray bedrock drill samples confirmed the absence of carbonates (<1 wt%) and the presence of clay and Ca-sulfate[12]. An association between CaO and sulfate is also clearly observed (Figure S3), suggesting no significant calcite is present in the Murray formation.

An interval with Mg-sulfates

In addition to Ca-sulfate, Mg-sulfate bedrock enrichments occur in a relatively thin (<10 m) stratigraphic interval within the heterolithic Sutton Island member (Figure 1-d; purple bar). On sol 1690 (elevation, -

4287 m), ChemCam analysis of unusual, brown-colored bedrock fragments within the Murray mudstone showed a distinct enhancement of Mg, S, and H. The estimated composition is interpreted as a binary mixture between a hydrated Mg-sulfate end-member and typical bedrock of the Murray formation (Figure 2-b,c and S1). The analyzed fragments have a bulk water content of 8.6 +/- 1.9 wt%, estimated from the hydrogen signal[21], which is significantly higher than typical Murray bedrock (1.6 wt%). The lack of Ca-sulfate enrichment in these rocks is reflected in a very low CaO content (Figure S1). The magnitude of the sulfur signal is consistent with $18.4^{+4.0}_{-4.8}$ wt% average sulfate content based on measurements of the Norwood Cove fragment (Figure S6) with 1-sigma uncertainty, corresponding to a bulk content of 33 wt% hydrated Mg-sulfate (1-sigma lower bound is 26 wt% ; Table S2).

Mg-sulfate enriched lithologies occur in planar exposures of relatively erosion-resistant rocks. The outcrop is poorly preserved, and consists of broken, meter-scale blocks separated by unconsolidated fines. Relative to surrounding lithologies, strata with Mg-sulfate enrichment have a reddish-brown color, are variably fractured, show a typical nodular to massive texture (Figure S7), and weather into centimeter-sized angular fragments (such as the Norwood Cove and Beach Cliff targets, see Figure S6). The grain size of these Mg-sulfate enriched rocks is silt-sized or smaller, on the basis of compositional homogeneity of the ChemCam data (Figure S8), and is similar to grain sizes estimated for surrounding Murray bedrock[22]. At several locations, this lithology is exposed in large contiguous blocks and confined to cm-thick planar exposures that are evenly interbedded with finely-laminated Murray mudstone (Figure 3-a). The lateral extent of Mg-sulfate-enriched exposures is uncertain because of the lack of high-resolution image coverage and the scattered nature of bedrock exposures (Figure S7). The maximum lateral distance observed in images is 4 m. Sporadic Mg-sulfate detections were also observed over 30 meters of thickness of heterolithic facies above (Figure 1-d).

The Mg-sulfate enriched rocks were not examined by the Alpha Particle X-ray Spectrometer (APXS), but high epithermal neutron count rates, recorded by the Dynamic Albedo of Neutrons (DAN) instrument in the same area (Figure S9), support the presence of elevated bedrock hydration within this stratigraphic interval. A signature consistent with a hydrated sulfate phase is also recorded on the site from orbit: hydration and hydrated sulfate spectral indices are enhanced in the portion of the Murray formation where Mg-sulfate enriched lithologies were observed *in situ*, and the signature was less clear or absent in bedrock exposures below that interval (Figure S11). The hydrated sulfate signature also extends laterally at similar elevation to either side of the rover traverse.

Timing of enrichment and formation scenario

Understanding the timing of bedrock sulfate enrichment is crucial to deciphering its environmental implication. Enrichments have not been observed in the form of large continuous beds of nearly pure salt, as could be expected for evaporite minerals formed as cumulates or as lake bottom-growth deposits. In available images of bedrock, no features were observed that clearly indicate primary salts, their dissolution, or the presence of disruptive fabrics common to terrestrial evaporitic settings[23].

Although a late diagenetic origin for Ca and Mg-sulfate enrichments cannot be uniquely discounted, we believe that such an origin is unlikely. Local bedrock does not appear to show a greater abundance of mineralized fractures (Figure 3, S4 and S5), and sulfate enrichments are disseminated in the host rock and do not correlate with the late-diagenetic fractures mineralized by Ca-sulfate[13] (Figure S5). Additionally, the presence of mineralized veins within typically sulfate-poor Murray bedrock suggests that bedrock porosity was sufficiently reduced that later diagenetic fluids were confined to fracture systems.

Early diagenetic precipitation from saline brines, followed by recrystallization during burial and exhumation, is in line with the observed geochemistry and textures. In particular, the disseminated sulfate

enrichments are restricted to a specific stratigraphic interval, where they occur as repetitive discrete horizons (Figure 3). In this scenario, episodic saturation of sulfate-rich brines resulted in the early diagenetic precipitation of sulfate salts within shallow sediments (Figure 4). Such subsurface crystallization can occur either during subaerial exposure resulting in evaporative enrichment in the capillary fringe, or subaqueously as dense supersaturated brines diffuse downward into the sediment pore space[24]. The estimated 30-50 wt% of Ca-sulfate enrichment is consistent with intrasediment crystallization in poorly compacted sediment[25]. Similar deposition could have occurred with Mg-sulfates where brines became much more concentrated by evaporation (Figure 4). The estimated proportion of 26-36 wt% Mg-sulfate initially represents 38-50% by volume, assuming precipitation of epsomite ($MgSO_4 \cdot 7H_2O$) in pores of siliciclastic sediment with grains of approximately basalt density (~3.0 $g.cm^{-3}$), again implying growth in poorly compacted sediments.

Sulfate enrichment within discrete beds of limited lateral extent in the heterolithic mudstone-sandstone facies indicate that salts were likely deposited along shallow lake margins, possibly within multiple ponds fed by distributive channel systems and groundwaters (Figure 4). Mg-sulfate enrichment, which is confined to relatively small stratigraphic intervals, occurs in horizons discretely separate from Ca-sulfate suggesting that Mg-sulfate rich brines were physically fractionated from the fluid that formed Ca-sulfates as the brine concentrated downstream. Changes in seasonal temperature and humidity cycling during post-depositional exposure of such hydrated sulfate salts would have exposed these materials to repeated changes in hydration state and dissolution. In the absence of complete dissolution, volumetric changes associated with changes in hydration state are expected to disrupt initial depositional textures[26,27].

After deposition, the Murray formation was likely buried to ~1 km[9], which itself may have triggered a change in Ca-sulfate hydration state[28,29]. Following compaction and lithification, late-stage fluids deposited Ca-sulfate within fractures. Horizontal and subhorizontal veins occur specifically in the

157 stratigraphic interval with the enrichments (Figure 1-c), a setting similar to terrestrial satin spar veins
158 associated to primary Ca-sulfate deposits[30]. These late Ca-sulfate fluids were likely to have partially
159 mobilized highly soluble salts within the bedrock such as halite. Indeed enhanced Na-chloride detections
160 occur at specific stratigraphic intervals (Figure 1-e, Figure S10), and their sporadic distribution in bedrock
161 and occasionally in association with fracture-filling Ca-sulfates indicate remobilization[31]. Locally, lateral
162 variation and possible cross-cutting of Mg-sulfate enrichment occurs at a cm-dm scale (Figure S7), as well
163 as sporadic detections of Mg-sulfate nearby the stratigraphic succession (Figure 1-d), may also reflect
164 localized dissolution and reprecipitation of initial deposits. (Figure 1-d). Yet, while Ca-sulfate-enriched
165 fluids would easily mobilize halite, Mg-sulfate-enriched bedrock could persist even though Mg-sulfate is
166 soluble, because SO_4^{2-} ions released during dissolution would immediately trigger the formation of less-
167 soluble Ca-sulfate, which could shield Mg-sulfates from further dissolution.

168 Upon exhumation and exposure of the Murray formation to temperatures and relative humidity of modern
169 Mars, hydrated Mg-sulfate minerals turn to amorphous phases of various hydration states. The calculated
170 21 wt% water associated with the Mg-sulfate phase (Figure 2-c; Table S2) corresponds to a hydration state
171 of 1.8 H_2O per $MgSO_4$, and is consistent with the predicted amorphous desiccation products of epsomite
172 or hexahydrite[26,32]. The intensely fractured and broken nature of Mg-sulfate enriched rocks may reflect
173 diurnal and seasonal cycles of dehydration-rehydration[33].

174 Overall, geochemical and textural data are consistent with sulfate enrichment in this interval by early
175 diagenetic precipitation from saline waters although unambiguous sedimentary structures (e.g., nodular
176 displacive fabrics) are not observed. This may result from the scarcity of high-resolution images acquired
177 in this interval or to the post-depositional alteration of primary depositional textures. Importantly,
178 however, features other than sulfate enrichments indicate lowering of lake levels and intermittent
179 evaporative conditions in this part of the Murray formation. First, desiccation cracks are identified in the

stratigraphy at Old Soaker[34] and possibly at several other locations (Figure 11) in close proximity to the strata containing sulfate enrichment (Figure 1-d). At Old Soaker, Ca-sulfate enrichment occurs in sandstone adjacent to the mudcracks (Figure 3-d). Second, elevated concentration of Na-chloride in the bedrock is also observed, relative to stratigraphically lower strata[31]. Na-chloride occurrences in specific intervals, close to sulfate enrichments suggests remobilization from layers potentially enriched in halite (Figure 1-e). Third, the first occurrence of Ca-sulfate enrichment coincides with a previously reported change in clay mineralogy, consistent with episodic wetting and drying of lake environments[12] and increased chemical weathering of the bedrock detrital component[18] (Figure 1). In Gale's closed-basin hydrology, leached ions would accumulate in waters and upon evaporation create brines that precipitate salts, such as Ca and Mg-sulfates.

Climatic variability

The observed Ca-/Mg-sulfate and chloride assemblages are predicted to result from alteration of Martian basalts to produce sulfate- and chloride-rich but iron-poor brines[1]. The relatively low solubility of Ca-sulfate minerals results in their widespread production during evaporation, while less common Mg-sulfate and chloride minerals represent terminal evaporation. Iron oxides are observed in visible/near-infrared spectral data and x-ray diffraction of Murray bedrock samples[28,35], yet there is no evidence for Fe-sulfate enrichments in this interval, likely because Fe was not mobile in solution, indicating that saline waters were either oxidizing or not acidic. While Ca-sulfate enrichment is observed, calcite is absent from the stratigraphy, i.e. not detected by CheMin at its threshold of 1 wt.%. This could result from either low alkalinity or low atmospheric CO_2, or an environment where precipitation of calcite was otherwise inhibited[36]. Besides, the presence of Ca-sulfate means prior $CaCO_3$ formation (if any) was insufficient to deplete Ca from solution. Our findings do not compromise the search for life in Gale crater; terrestrial Mg

sulfate-rich hypersaline lakes are known to accommodate halotolerant biota[37–39] and crystallization of sulfate salts may also aid preservation of biosignatures[40].

Previous observations suggest different lake depths were recorded in the lower Murray formation[10]. In the upper part of the formation, where clear rock exposures are more scarce, sedimentary structures suggest deposition in lake-margin environment with potential episodes of desiccation[34,41,42]. Our discovery of sulfate deposits is consistent with episodic dessication. The limited lateral extent of sulfate-enriched beds also suggests the potential for segmentation of the Gale lake into discrete ponds, including those where extremely evapo-concentrated brines might form (Figure 4). Changes in lake level are an anticipated response within closed basin lakes to variation in the regional hydrological budget. In addition, over time intervals for lacustrine deposition of ~1 Ma or less, based on plausible sedimentary deposition rates[9], Mars experiences significant changes in obliquity and orbital eccentricity driving cyclical climate fluctuations[43]. Alternatively, a drier lake Gale might be a sign of long-term, secular global drying of Mars, posited based on orbital observations[5].

The interval discussed here preserves the first occurrence of significant sulfate-enriched bedrock (>30 wt% sulfate with siliciclastics) in Gale crater's sedimentary record. As the rover continues to traverse upsection toward successively younger rocks, key questions include the prevalence of similar bedrock sulfate enrichments. If thin stratigraphic intervals with salt enrichments or sedimentological evidence for aridity continue to occur, cyclical or episodic processes are a plausible underlying cause. If, on the other hand, sulfate enriched intervals increase in frequency and thickness, perhaps incorporating observable displacive fabrics and pure sulfate beds, the enrichments investigated here may be a harbinger of the long term, secular drying of Mars. This has been hypothesized for the Mt. Sharp sulfate unit observed from orbit further upsection[8] and deposits elsewhere on Mars[5]. As the rover continues its traverse towards this sulfate unit, it will be therefore crucial to recognize sulfate-enriched bedrock in reconnaissance

observations, so as to obtain accompanying high resolution stereo images of textures and drill samples for x-ray diffraction, evolved gas, and isotopic analyses.

References

1. Tosca, N. J. & McLennan, S. M. Chemical divides and evaporite assemblages on Mars. *Earth Planet. Sci. Lett.* **241**, 21–31 (2006).
2. Clark, B. C. *et al.* Chemistry and mineralogy of outcrops at Meridiani Planum. *Earth Planet. Sci. Lett.* **240**, 73–94 (2005).
3. Tosca, N. J. *et al.* Geochemical modeling of evaporation processes on Mars: Insight from the sedimentary record at Meridiani Planum. *Earth Planet. Sci. Lett.* **240**, 122–148 (2005).
4. Ehlmann, B. L. & Edwards, C. S. Mineralogy of the Martian Surface. *Annu. Rev. Earth Planet. Sci.* **42**, 291–315 (2014).
5. Bibring, J.-P. *et al.* Global Mineralogical and Aqueous Mars History Derived from OMEGA/Mars Express Data. *Science* **312**, 400–404 (2006).
6. Le Deit, L. *et al.* Sequence of infilling events in Gale Crater, Mars: Results from morphology, stratigraphy, and mineralogy. *J. Geophys. Res. Planets* **118**, 2439–2473 (2013).
7. Fraeman, A. A. *et al.* The stratigraphy and evolution of lower Mount Sharp from spectral, morphological, and thermophysical orbital data sets. *J. Geophys. Res. Planets* **121**, 1713–1736 (2016).
8. Milliken, R. E., Grotzinger, J. P. & Thomson, B. J. Paleoclimate of Mars as captured by the stratigraphic record in Gale Crater. *Geophys. Res. Lett.* **37**, @CitationL04201-@CitationL04201 (2010).
9. Grotzinger, J. P. *et al.* Deposition, exhumation, and paleoclimate of an ancient lake deposit, Gale crater, Mars. *Science* **350**, aac7575 (2015).

10. Hurowitz, J. A. *et al.* Redox stratification of an ancient lake in Gale crater, Mars. *Science* **356**, eaah6849 (2017).
11. McLennan, S. M. *et al.* Elemental Geochemistry of Sedimentary Rocks at Yellowknife Bay, Gale Crater, Mars. *Science* **343**, 1244734 (2014).
12. Bristow, T. F. *et al.* Clay mineral diversity and abundance in sedimentary rocks of Gale crater, Mars. *Sci. Adv.* **4**, eaar3330 (2018).
13. Nachon, M. *et al.* Calcium sulfate veins characterized by ChemCam/Curiosity at Gale crater, Mars. *J. Geophys. Res. Planets* **119**, 2013JE004588 (2014).
14. Rapin, W. *et al.* Hydration state of calcium sulfates in Gale crater, Mars: Identification of bassanite veins. *Earth Planet. Sci. Lett.* **452**, 197–205 (2016).
15. Kah, L. C., Stack, K. M., Eigenbrode, J. L., Yingst, R. A. & Edgett, K. S. Syndepositional precipitation of calcium sulfate in Gale Crater, Mars. *Terra Nova* **30**, 431–439 (2018).
16. Nachon, M. *et al.* Chemistry of diagenetic features analyzed by ChemCam at Pahrump Hills, Gale crater, Mars. *Icarus* **281**, 121–136 (2017).
17. VanBommel, S. J. *et al.* Deconvolution of distinct lithology chemistry through oversampling with the Mars Science Laboratory Alpha Particle X-Ray Spectrometer. *X-Ray Spectrom.* **45**, 155–161 (2016).
18. Mangold, N. *et al.* Chemical alteration of fine-grained sedimentary rocks at Gale crater. *Icarus* **321**, 619–631 (2019).
19. Anderson, D. E. *et al.* Characterization of LIBS emission lines for the identification of chlorides, carbonates, and sulfates in salt/basalt mixtures for the application to MSL ChemCam data. *J. Geophys. Res. Planets* **122**, 744–770 (2017).
20. Stack, K. M. *et al.* Evidence for plunging river plume deposits in the Pahrump Hills member of the Murray formation, Gale crater, Mars. *Sedimentology* **0**, (2018).

21. Rapin, W. *et al.* Quantification of water content by laser induced breakdown spectroscopy on Mars. *Spectrochim. Acta Part B At. Spectrosc.* **130**, 82–100 (2017).
22. Rivera-Hernández, F. *et al.* Using ChemCam LIBS data to constrain grain size in rocks on Mars: Proof of concept and application to rocks at Yellowknife Bay and Pahrump Hills, Gale crater. *Icarus* **321**, 82–98 (2019).
23. Warren, J. K. *Evaporites:Sediments, Resources and Hydrocarbons*. (Springer Science & Business Media, 2006).
24. Handford, C. R. Chaper 1 Marginal Marine Halite: Sabkhas and Salinas. in *Developments in Sedimentology* (ed. Melvin, J. L.) **50**, 1–66 (Elsevier, 1991).
25. Giles, M. R. Diagenesis: A quantitative perspective: Implications for basin modelling and rock property prediction. (Kluwer Academic Pub, 1997).
26. Chipera, S. J. & Vaniman, D. T. Experimental stability of magnesium sulfate hydrates that may be present on Mars. *Geochim. Cosmochim. Acta* **71**, 241–250 (2007).
27. Holliday, D. W. The petrology of secondary gypsum rocks; a review. *J. Sediment. Res.* **40**, 734–744 (1970).
28. Vaniman, D. T. *et al.* Gypsum, bassanite, and anhydrite at Gale crater, Mars. *Am. Mineral. J. Earth Planet. Mater.* **103**, 1011–1020 (2018).
29. Schieber, J. *et al.* Encounters with an unearthly mudstone: Understanding the first mudstone found on Mars. *Sedimentology* **64**, 311–358 (2017).
30. Gustavson, T. C., Hovorka, S. D. & Dutton, A. R. Origin of satin spar veins in evaporite basins. *J. Sediment. Res.* **64**, 88–94 (1994).
31. Thomas, N. H. *et al.* MSL ChemCam Observations of Chloride Salts in Gale Crater, Mars. in **49**, 2876 (2018).

32. Wang, A., Freeman, J. J. & Jolliff, B. L. Phase transition pathways of the hydrates of magnesium sulfate in the temperature range 50°C to 5°C: Implication for sulfates on Mars. *J. Geophys. Res. Planets* **114**, E04010 (2009).
33. Vaniman, D. T. & Chipera, S. J. Transformations of Mg- and Ca-sulfate hydrates in Mars regolith. *Am. Mineral.* **91**, 1628–1642 (2006).
34. Stein, N. *et al.* Desiccation cracks provide evidence of lake drying on Mars, Sutton Island member, Murray formation, Gale Crater. *Geology* **46**, 515–518 (2018).
35. Johnson, J. R. *et al.* Chemcam Passive Reflectance Spectroscopy of Recent Drill Tailings, Hematite-Bearing Rocks, and Dune Sands. in **47**, 1155 (2016).
36. Tosca, N. J., Ahmed, I. A. M., Tutolo, B. M., Ashpitel, A. & Hurowitz, J. A. Magnetite authigenesis and the warming of early Mars. *Nat. Geosci.* **11**, 635 (2018).
37. Cabestrero, Ó., del Buey, P. & Sanz-Montero, M. E. Biosedimentary and geochemical constraints on the precipitation of mineral crusts in shallow sulphate lakes. *Sediment. Geol.* **366**, 32–46 (2018).
38. Kilmer, B. R. *et al.* Molecular and Phenetic Characterization of the Bacterial Assemblage of Hot Lake, WA, an Environment with High Concentrations of Magnesium Sulfate, and Its Relevance to Mars. *Int. J. Astrobiol.* **13**, 69–80 (2014).
39. Pontefract, A. *et al.* Microbial Diversity in a Hypersaline Sulfate Lake: A Terrestrial Analog of Ancient Mars. *Front. Microbiol.* **8**, 1819 (2017).
40. Aubrey, A. *et al.* Sulfate minerals and organic compounds on Mars. *Geology* **34**, 357–360 (2006).
41. Fedo, C. *et al.* Sedimentology and Stratigraphy of the Murray Formation, Gale Crater, Mars. in **49**, 2078 (2018).
42. Schieber, J. *et al.* A Sand-Lens in the Upper Murray Formation at Gale Crater, Mars: A Likely Lowstand Deposit of a Dynamic Ancient Lake. in **48**, 2311 (2017).

43. Laskar, J. *et al.* Long term evolution and chaotic diffusion of the insolation quantities of Mars. *Icarus* **170**, 343–364 (2004).

Corresponding author: wrapin@caltech.edu

Acknowledgements: Thanks to the MSL operations team for their dedication in generating this dataset and to the LANL team for collection of data to support sulfur calibration. Thanks to John Grotzinger, Chris Fedo, Kirsten Siebach, Lauren Edgar, and other members of the informal MSL Sed-Strat group for discussions which helped improve this work. The authors also thank Sam Clegg and other members of the ChemCam team for discussions on the sulfur signal calibration. We also thank Nick Tosca and two anonymous reviewers for their helpful comments. W.R. and B.L.E. were funded by a MSL Participating Scientist grant to B.L.E. The work of G.D. was supported by the CNES through the ChemCam Program. This work and the MSL project is supported by the NASA Mars Exploration Program.

Author contributions: W.R. analyzed data, conceived and wrote the manuscript; B.L.E. and G.D. conceived and revised the manuscript; J.S., W.W.F., B.C.C., L.C.K., N.M., R.C.W. and A.R.V., contributed to the interpretation of the data and revisions of the manuscript; N.H.T. provided Cl peak analysis; V.K.F. analyzed CRISM signatures of hydrated sulfates; N.T.S. and F.R.H. provided grain size estimates from MAHLI images of Murray bedrock; M.N. and H.A.M. identified and mapped sulfate veins occurrences; L.T. analyzed APXS data of Murray bedrock; T.S.J.G and C.H. provided DAN data analysis.

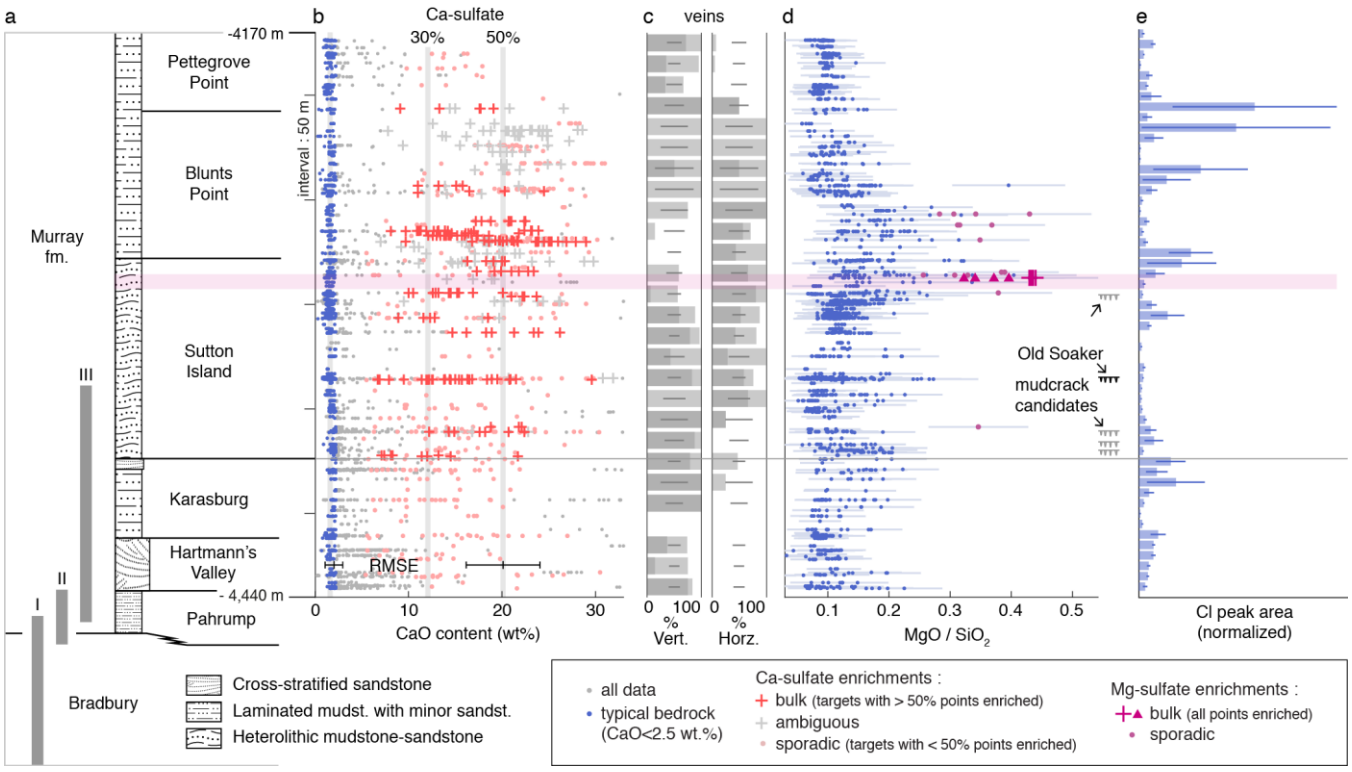

Figure 1: **Stratigraphic context on bedrock composition. a**, Overview of the ~350 m of stratigraphy explored *in situ* at Gale crater including dominant facies observed[41] and sections highlighting evidence for: I, fluvio-lacustrine environment[9]; II, lake redox stratification[10]; III, increase of bedrock chemical weathering upsection due to leaching of Ca-bearing mafic minerals[18]. **b**, Bedrock CaO content with bulk (crosses), or sporadic (dots) enrichments. Grey crosses represent bulk enriched targets but which distinction to fracture-fill veins remains ambiguous from available images. Vertical grey lines highlight average bedrock composition (1.6 wt% CaO), with 30% and 50% Ca-sulfate (bassanite) enrichments. **c**, Occurrence of fracture-fill veins for vertical and horizontal orientations as percent of the number of workspace images with bedrock (Figure S12). Light-grey indicates at least a vein is visible and dark grey correspond to higher density of veins; horizontal bars represent the uncertainty of the average. **d**, Bedrock MgO/SiO_2 content ratio (same data as Figure 2-b,c). Error bars represent RMSE for the ratio of MgO and SiO_2 content. The purple horizontal bar represents the elevation range where Mg-sulfate enriched

lithology is observed (Figure S7). Location of Old Soaker[34] and other candidate desiccation cracks (Figure S13). **e**, Average normalized Cl peak area associated with halite detections (Figure S10)[31], error bar represents the uncertainty of the average.

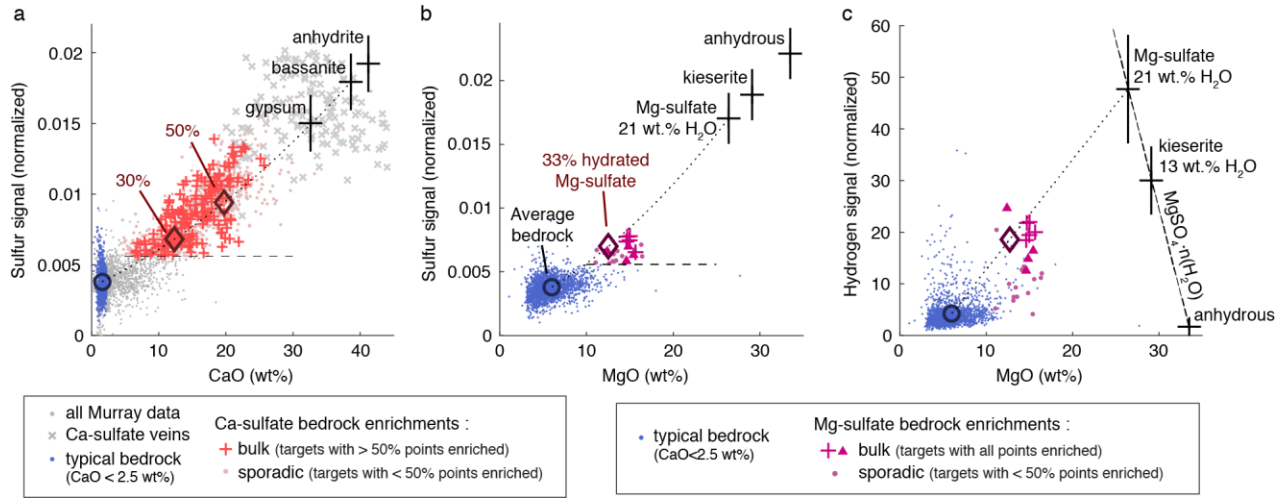

Figure 2: **ChemCam oxide and elemental data of Ca- and Mg-sulfate enrichments.** Sulfur signal as a function of CaO (**a**) and MgO content (**b**), and hydrogen signal as a function of MgO content, for typical Murray bedrock with CaO < 2.5 wt% (blue) and for sulfate enrichments. **a**, For Ca-sulfates (red), sulfur signal above the limit of detection (dashed line, SO_3 > 10.6 wt%) and CaO>5wt%. Mixtures at 30% and 50% (diamonds) of Ca-sulfate with average typical bedrock (circle) are shown with the binary mixing trend (dotted line) and end-members (black crosses). **b-c**, Mg-sulfate enrichments (purple), defined by sulfur signal above the limit of detection and MgO > 10 wt%, found disseminated in the Norwood Cove (crosses) and Beach Cliff (triangle) bedrock fragments (Figure S6), and compared to 33% hydrated Mg-sulfate mixture (diamond) with average bedrock (Table S2). **c**, Dashed line represents Mg-sulfate with varying water content. Vertical error bars on end-members represent sulfate (**a**,**b**) and water content (**c**) calibration uncertainties.

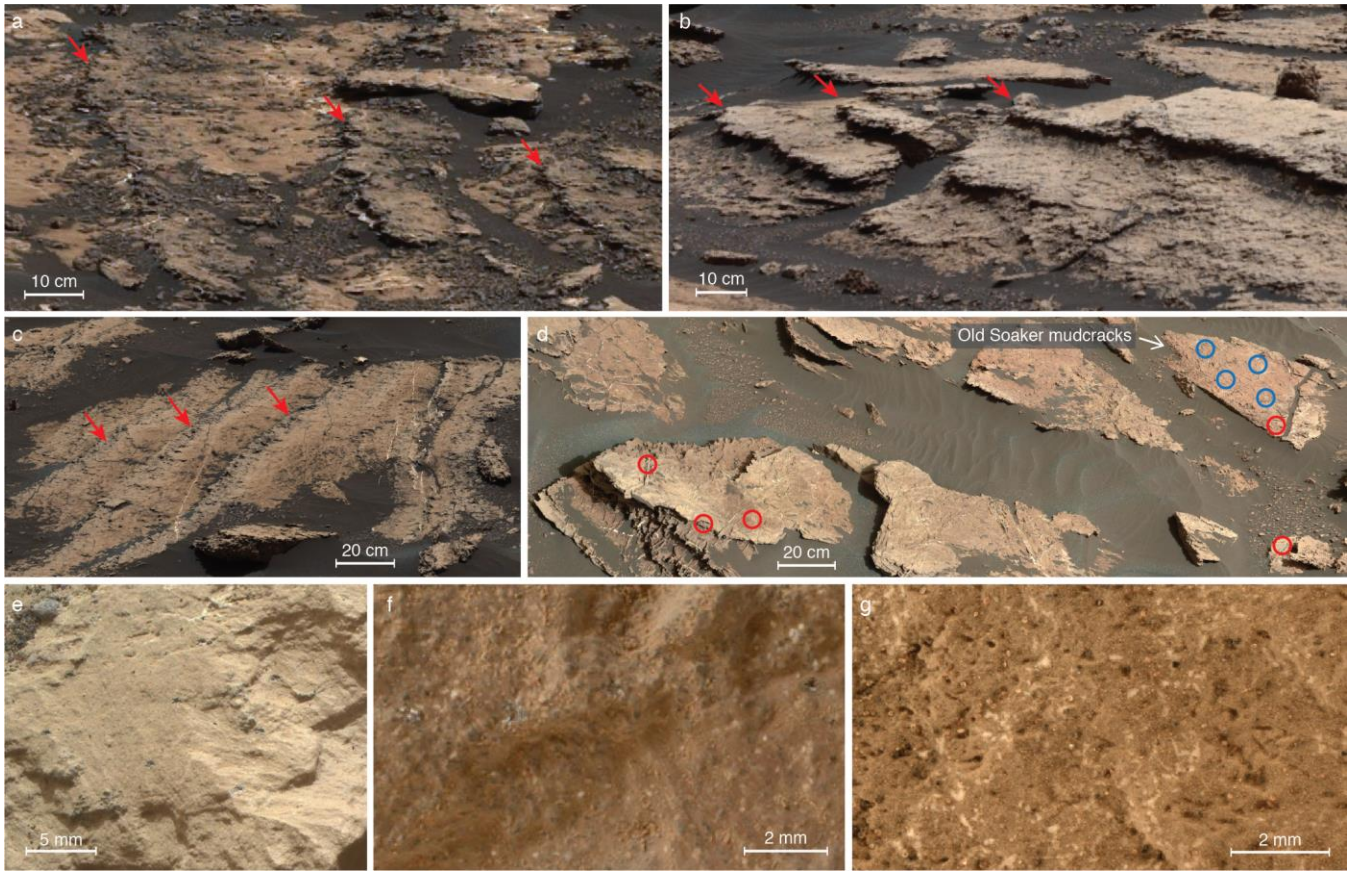

Figure 3: **Lithology of the sulfate enrichments. a**, Mg-sulfate enriched lithology within multiple parallel horizons (red arrows) on a large block of bedrock (mcam08715). **b**, Ca-sulfate enrichments as erosion-resistant horizons (red arrows) in mudstone (mcam08669; Figure S4-a). **c**, Multiple horizons (red arrows) where euhedral white crystals (Figure S4-g) and heterogeneous Ca-sulfate and Mg-sulfate enrichments were observed (mcam08733). **d**, Exposed blocks at Old Soaker with desiccation cracks[34] (Figure S13-a) (mcam07752); circles represent the locations of ChemCam targets with Ca-sulfate enrichments (red) and without (blue). Close-up MAHLI images of a mudstone (**e**, Lookout Point, Figure S5-a) and a sandstone enriched in Ca-sulfate (**f**, 1710MH0001220010604335C00; White Ledge, Figure S5-c). **g**, Close-up MAHLI image of bedrock with white euhedral crystals along with empty casts/molds (1679MH0001930000603555R00; Figure S4-d).

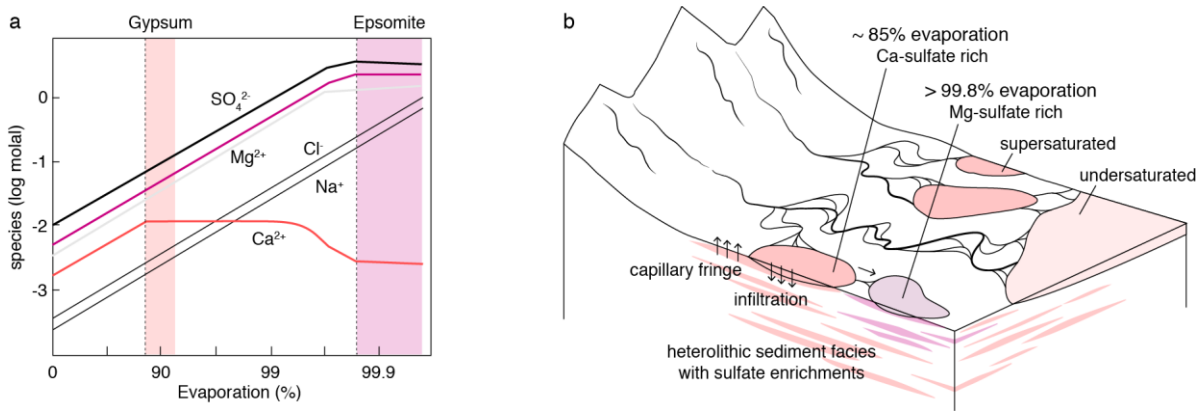

376

377 Figure 4: **Evaporation of surface brines and early diagenetic deposition**. **Left**, Evaporation of basaltic
378 weathering-derived fluids leads to major precipitation of Ca-sulfates first like gypsum (red) and then Mg-
379 sulfates like epsomite (purple) within the shaded ranges of evaporation, after Tosca et al. (2005)[3]. The
380 evolution of Fe species, which are dependent on pH, does not significantly change the result on Ca- and
381 Mg-sulfate precipitation[3] and are not shown here because Fe is relatively immobile (found in iron oxides,
382 clays, and amorphous phases). **Right**, Deposition scenario in the margin of the Gale lake basin, possibly
383 forming several over-filled or evaporative ponds fed by distributive fluvial systems consistent with the
384 heterolithic mudstone-sandstone facies observed in the upper Murray formation[41]. Brine crystallizes in the
385 shallow sediment pore space either by subaqueous infiltration, or within capillary fringes where occasional
386 subaerial exposure occurs.

387

Methods

Rover-based geochemical datasets and data processing. MSL has 5 instruments that can measure geochemistry and mineralogy[44]. Because of the rover traverse path and rate at the time, APXS, CheMin, and SAM data were not acquired of the Mg-S-H enriched strata so ChemCam is the primary source of chemical data used along with hydration of the upper ~0.5 m of the surface probed by the DAN instrument. The latter is a neutron spectrometer, sensitive to thermal and epithermal neutrons, which is regularly operated in active and passive modes throughout the traverse. The count rate of thermal neutrons in passive mode (data shown in Figure S9) can be elevated either due to the presence of neutron scatterers (predominantly H) or the paucity of neutron absorbers (predominantly Cl and Fe)[45]. On the other end, ChemCam is a laser-induced breakdown spectrometer (LIBS) that provides chemical analyses at a submillimeter scale and detailed images with the Remote Micro Imager (RMI)[46,47]. Major-element contents were obtained using the current calibration model[48]. Water and sulfate contents were estimated using dedicated calibration models, see Rapin et al. (2017)[21] for water content quantification using the hydrogen signal, and see below a description of the sulfur signal calibration used in this study.

The ChemCam dataset used here includes bedrock targets of the Murray formation. A subset of bedrock observations was selected from all ChemCam observations based on: 1) image classification to select only bedrock analyses and remove potential contribution from soils or diagenetic features such as light-toned fracture-fill veins, 2) signal strength to keep points above a minimum total spectral intensity (more than 1.6 10^{14} photons) for which noise level is acceptable for sulfur peak analyses. An additional selection is made based on major-element oxide contents to separate points that indicate contributions from Ca-sulfate-, silica- or iron-rich features in order to represent typical bedrock composition (Figure 2, Figure S1). The threshold for rejection due to Ca-sulfate enrichment was defined at 2.5 wt% CaO from the distribution of bedrock observations which shows that measurements group tightly around 1.6 wt% CaO

with sporadic enrichments above 2.5 wt% (Figure S3) related to increased S signal (Figure S2). The APXS instrument independently measures centimeter-scale bulk compositions and demonstrates the association of calcium and sulfur in Murray bedrock observations. The CaO content measured by APXS ranges from 2 wt% to 25 wt% and is correlated with SO_3 content along the 1:1 stoichiometric ratio of Ca-sulfate (Figure S3). Given the correlation observed on APXS data down to 2 wt% CaO, the slightly lower CaO abundance of the cluster defined by ChemCam data is most likely related to its ability to examine bedrock free of dust and without Ca-sulfate enrichments with its 0.3-0.5 mm analytical footprint compared to the 17 mm footprint of APXS.

Estimation of sulfate content from ChemCam data. SO_3 content is estimated from the sulfur signal observed in ChemCam spectra. The challenge with the measurement of the signal is that the sulfur emission peaks present in ChemCam spectra are relatively weak in comparison to nearby interfering iron emission peaks[13], necessitating a distinct method for their quantification compared to the major oxides. Others have investigated the calibration of S with LIBS[49–51], here we used a distinct approach dedicated to data collected *in situ* on sulfates within the Murray bedrock. The approach is first to show from laboratory data that spectral parameters can be defined to identify and differentiate the sulfur signal from other interfering spectral features, including identification of the threshold of S wt. % at which it becomes apparent. Second, the sulfur signal identified on Mars is calibrated *in situ* using a large set of Murray bedrock measurements containing Ca-sulfate enrichments.

Collection of laboratory reference spectra. The ChemCam testbed at Los Alamos National Laboratory was used to collect data from pelletized mixtures of Ca-sulfates and Mg-sulfate with basalt as described in Anderson et al. (2017)[19]. Additional Mg-sulfate pressed pellets were also prepared to resolve sulfur signal variation closer to the limit of detection and compositional range observed in the enrichments at Gale crater. The same basalt as Anderson et al. (2017)[19] was used –K1919 basalt sieved powder (< 45

434 µm)– but it was doped with 7 wt% sieved hematite powder (< 45 µm) so that the mixture had a total iron
435 content of 19 wt%, closer to the bedrock composition of the Murray formation at Gale crater. The Mg-
436 sulfate powder was synthetic reagent, the same as used in [19] from Macron Chemicals (CAS 7487-88-9),
437 and was mixed in various proportions with the basalt-hematite powder (Table S3). The powder mixture
438 pellets were each analyzed with 8 observation points of 30 laser shots each.

439 *Processing and measurement of S emission peaks.* Iron peaks interfere significantly with the sulfur
440 emission peaks at ~543 nm (S II at 543.02 nm and S II at 543.43 nm forming a single peak in ChemCam
441 spectra) and 545.53 nm, but the sulfur still produces specific spectral peak features when present. The
442 sulfur signal can be distinguished using the position of the spectral peak centroid computed from,
443 respectively, 10 and 11 spectral bins on the two specific locations after baseline correction (Figure S14).
444 The sulfur emission peak area at ~564 nm (multiple S II peaks forming a single peak in ChemCam spectra),
445 with minor Si and Fe emission peaks interferences, is then used to evaluate sulfur signal intensity. It is
446 normalized to the oxygen emission peak area at ~778 nm (O I at 777.41 nm, 777.63 nm and 777.75 nm
447 forming a single peak). Sulfur and oxygen peak areas are obtained by integrating the spectral bins after
448 baseline correction. As shown on figure 2 the increase of sulfate abundance and associated decrease of
449 emission of other peaks from breakdown of the basalt matrix produces a specific shift to longer
450 wavelengths for the spectral centroids at ~543 nm and ~545 nm, while simultaneously the normalized
451 peak area at ~564 nm increases. Using this approach, laboratory data suggest a threshold of sulfate
452 detectability around 10 wt% sulfate with the possibility of obtaining a still lower threshold by more refined
453 fitting and/or multivariate spectral fitting procedures.

454 *Calibration of the S signal.* The S abundance estimates based on 564 nm peak area are calibrated with *in*
455 *situ* sulfate data collected on Mars. Indeed, bedrock of the upper Murray formation has a rather low bulk
456 CaO content, but a large number of CaO enrichments were observed at the LIBS scale, related to Ca-

sulfates. The S association with Ca is observed as the data from Murray bedrock, after removal of other Fe and Mg-rich diagenetic features, follows the same trend of peak area increase at ~564 nm and centroid shifts observed in the laboratory. Additionally, measurements from the APXS instrument independently confirm the correlation of CaO with SO_3 content in the upper Murray formation (Figure S3). The SO_3 content calibration curve for the normalized peak area at ~564 nm (Figure 2-f) is obtained by attributing CaO enrichments from average bedrock above 2.5 wt% CaO to Ca-sulfate.

This *in situ* calibration curve obtained using Ca-sulfate data can then be used to predict sulfate content related to Mg-sulfates because tests in the laboratory have shown that for both Mg-sulfates and Ca-sulfates the normalized peak area increases along the same calibration curve and up to the same normalized peak area value for the pure sulfate pellets (Figure 2-c). The limit of detection on sulfate content using this approach is calculated from the 95% confidence bound of the calibration curve. Its intercept has a normalized peak area which corresponds to a predicted 10.6 wt% SO_3 content. Data from upper Murray shows that MgO enrichments are correlated with the normalized S peak area at ~ 564 nm, as well as centroid shifts (Figure 2), which confirm the presence of sulfate from the signal. The current calibration model to estimate major oxide contents[48] is not optimized yet to include Mg-sulfate bearing basaltic mixtures, and consequently, the total amount of oxides predicted exceeds 100% after water and sulfate contents are included. This was also found to be the case when laboratory Mg-sulfate bearing basaltic mixture major elements were calculated using the current calibration model. Consequently, assuming the proportions predicted for the major oxides are correct, the oxide amounts are then renormalized to account for water and sulfate content, so that totals equal 100%.

Identification of the Mg-sulfate enriched lithology. A correlation was identified between the occurrence of Mg sulfates in LIBS data on sol 1680 (Figure 5) and the specific lithology observed on Murray bedrock in color image data (Figure S7). MastCam images of bedrock or blocks of bedrock were analyzed to

identify the Mg-sulfate enriched lithology with characteristics defined by its 1) texture: nodular or massive, erosion resistant, forming centimeter-thick layers in some cases, 2) weathering style: cracking in poorly rounded centimeter-sized chunks which remain more resistant to erosion than typical Murray bedrock, 3) color: brown relative to typical Murray bedrock. The specific color was identified and mapped on MastCam images to verify the same color was observed on the lithology at the different visited sites.

Color identification. RGB pixel values of the radiometrically corrected MastCam images were converted into CIE L*a*b* color space, with L* lightness, and a* and b* color parameters (Figure S15). This determined the color and lightness parameters interval for the fragments of bedrock where the Mg-sulfate enrichments were analyzed with LIBS. The interval then was used as a guide to map areas of the bedrock not measured by LIBS, with color and lightness parameters characteristic of the Mg-sulfate enrichments. The lithology is also identified from texture, morphology and weathering style in addition to this color-mapping technique.

Orbital data analysis. The Compact Reconnaissance Imaging Spectrometer for Mars (CRISM) onboard the Mars Reconnaissance Orbiter collects targeted hyperspectral images of the surface with spatial resolution between 12 and 18 m/pixel. Absorption features due to atmospheric carbon dioxide are removed using the Volcano scan method[52]. The Discrete Ordinate Radiative Transfer model[53] is used to account for effects due to temporally and spatially variable atmospheric dust and ice aerosols. The observations shown on Figure S11 are map-projected and spectrally smoothed using an iterative log likelihood algorithm to incorporate the instrument's spatial and spectral transfer functions to retrieve the best estimate of the surface albedo in the presence of Poisson-distributed noise and spatial blur[54]. A Spectral absorption at 1.9 µm is indicative of H_2O within a hydrated mineral and convexity at 2.29 µm measures the dual presence of the broad hydration absorption and the S-O bending or mineral H_2O overtone commonly observed in hydrated sulfates[55]. Spectra are extracted from spatial regions of interest as determined by

the spatial parameterization, and spectral features are compared to those of laboratory standards to confirm mineral identifications.

Mapping of vein distribution. The presence of veins was mapped along the traverse using MastCam end-of-drive imaging of the surface in front of the rover. The area covered by the images is divided into typically 4 areas covering ~4 m^2 of Martian surface. In each area covering bedrock, the presence of veins is reported in vertical and horizontal categories depending on their apparent orientation being either close to vertical or horizontal. In addition, reference cases of dense vein networks are used to report qualitatively the presence of higher density for veins either vertical or horizontal (Figure S12).

Data availability: All *in situ* and orbital data used in this study are available in the NASA Planetary Data System (pds-geosciences.wustl.edu). All other supplementary data that support the findings of this study are available from the corresponding author upon request.

Methods references

44. Grotzinger, J. P. *et al.* Mars Science Laboratory Mission and Science Investigation. *Space Sci. Rev.* **170**, 5–56 (2012).
45. Mitrofanov, I. *et al.* Studying of water consent in Mars' gale crater: The first results of the DAN experiment on the NASA curiosity rover. *Dokl. Phys.* **59**, 126–128 (2014).
46. Maurice, S. *et al.* The ChemCam Instrument Suite on the Mars Science Laboratory (MSL) Rover: Science Objectives and Mast Unit Description. *Space Sci. Rev.* **170**, 95–166 (2012).
47. Wiens, R. C. *et al.* The ChemCam Instrument Suite on the Mars Science Laboratory (MSL) Rover: Body Unit and Combined System Tests. *Space Sci. Rev.* **170**, 167–227 (2012).

48. Clegg, S. M. *et al.* Recalibration of the Mars Science Laboratory ChemCam instrument with an expanded geochemical database. *Spectrochim. Acta Part B At. Spectrosc.* **129**, 64–85 (2017).
49. Dyar, M. D. *et al.* Strategies for Mars remote Laser-Induced Breakdown Spectroscopy analysis of sulfur in geological samples. *Spectrochim. Acta Part B At. Spectrosc.* **66**, 39–56 (2011).
50. Schröder, S., Pavlov, S. G., Rauschenbach, I., Jessberger, E. K. & Hübers, H.-W. Detection and identification of salts and frozen salt solutions combining laser-induced breakdown spectroscopy and multivariate analysis methods: A study for future martian exploration. *Icarus* **223**, 61–73 (2013).
51. Sobron, P., Wang, A. & Sobron, F. Extraction of compositional and hydration information of sulfates from laser-induced plasma spectra recorded under Mars atmospheric conditions — Implications for ChemCam investigations on Curiosity rover. *Spectrochim. Acta Part B At. Spectrosc.* **68**, 1–16 (2012).
52. McGuire, P. C. *et al.* An improvement to the volcano-scan algorithm for atmospheric correction of CRISM and OMEGA spectral data. *Planet. Space Sci.* **57**, 809–815 (2009).
53. Stamnes, K., Tsay, S.-C., Wiscombe, W. & Laszlo, I. DISORT, a general-purpose Fortran program for discrete-ordinate-method radiative transfer in scattering and emitting layered media: documentation of methodology. (2000).
54. He, L., O'Sullivan, J., Politte, D. & Arvidson, R. Resolution Analysis of Regularized Maximum Log-likelihood Reconstruction Method for CRISM Hyperspectral Data. in *Propagation Through and Characterization of Atmospheric and Oceanic Phenomena* JTu5A–16 (Optical Society of America, 2017).
55. Cloutis, E. A. *et al.* Detection and discrimination of sulfate minerals using reflectance spectroscopy. *Icarus* **184**, 121–157 (2006).